On the function of lead (Pb) in machining brass alloys

N.B. When citing this work, cite the original published paper.

(article starts on next page)

ORIGINAL ARTICLE

On the function of lead (Pb) in machining brass alloys

Jakob Johansson[1] · Per Alm[2] · Rachid M'Saoubi[1,2] · Per Malmberg[3] · Jan-Eric Ståhl[1] · Volodymyr Bushlya[1]

Abstract

Lead has traditionally been added to brass alloys to achieve high machinability, but the exact mechanisms at work are still debated. Lead-free brass alternatives could be developed if these mechanisms were better understood. Accordingly, machinability characteristics were investigated for two brass alloys with similar mechanical properties and phase composition, but with very different machining characteristics because one has 3 wt.% lead (CuZn38Pb3) while the other has only 0.1 wt.% (CuZn42). The effect of the lead was investigated using infrared temperature measurement, electron microscopy, secondary ion mass spectroscopy, quick-stop methods, and high-speed filming. Neither melting of lead nor its deposition on the tool rake surface takes place during machining thus confirming its limited lubrication and tribological effects. Instead, the main role of lead is to promote discontinuous chip formation. Lead deforms to flake-like shapes that act as crack initiation points when the workpiece material passes through the primary deformation zone. This effect prevents the development of stable tool–chip contact, thus lowering cutting forces, friction, and process temperature.

Keywords Machining · Lead · Brass alloys · Chip formation

1 Introduction

Lead (Pb) has traditionally been added to brass alloys to make the machining processes easier and more efficient [1]. However, due to lead's detrimental effect on human health, the use of lead is becoming more restricted in several regions worldwide [2–4]. Since lead-containing alloys cannot be used in certain applications, it is necessary to move to lead-free alternatives. Unfortunately, the existing lead-free brass alloys lack the machinability of leaded brass alloys [5–8]. Alternative ways of improving the machinability of lead-free brass alloys have been explored, i.e., by alloying brass with bismuth, selenium, indium, and graphite [9–11], but these alloys are yet to be implemented for industrial manufacturing. While there are a number of contradictory opinions on the function of lead in machining, there is a consensus that it improves process outcomes [1, 12–15].

(i) Excellent chip control and chip breaking

A characteristic feature of machining leaded brass is the extremely favorable chip form with small, discontinuous chip segments. Under reasonable production conditions, no continuous chips will be formed regardless of depth of cut and feed [16]. Traditionally, the type of chips formed (continuous, segmented, discontinuous) is linked to the mechanical and thermal properties of the workpiece material [17]. When using standard tensile testing protocols, similar mechanical properties are found for brasses with similar phase compositions but with different lead content. However, the behavior of these alloys when machining is quite different. There is a large difference in strain rate between tensile testing and metal cutting. In tensile testing, strain rates of less than 0.01 s^{-1} are used (ISO 6892–1), while for metal cutting strain rates in the order of $2 \times 10^4 \text{ s}^{-1}$ or more are normal [18]. Hofmann and El-Magd [19] have shown that leaded and lead-free brass behave differently at high strain rates — leaded brass alloys exhibit lower ductility at high strain rates. Doyle [20] attributed the discontinued chip formation in

✉ Jakob Johansson
jakob.johansson@iprod.lth.se

1 Division of Production and Materials Engineering, Lund University, Lund, Sweden

2 R&D Materials and Technology Development, Seco Tools AB, Fagersta, Sweden

3 Chemistry and Chemical Engineering, Chalmers University of Technology, Gothenburg, Sweden

Ⓓ Springer

leaded brass to a ductile rupture process instigated in segregated lead grains in the alloy. Low ductility, in general, is known to facilitate discontinuous chip formation, as in the case of bronze and cast iron machining [17].

(ii) Low cutting forces

It is well documented that brass alloyed with lead results in lower cutting forces than for lead-free variants [21, 22]. In 1979, Stoddart et al. [23] used Auger electron spectroscopy to demonstrate that lead forms a thin film on the side of the chip that slides against the cutting tool. The authors suggested that the lead layer forms and replenishes on the tool–chip interface, so contributing to lubrication, cooling of the cutting edge, and reduction of forces. Gane [24] further investigated friction in machining of leaded and lead-free brass, using both cutting and sliding experiments. His experiments showed that the friction stress for leaded brass was about half that measured for brass without lead. The author proposed that the reduced cutting forces when cutting leaded brass could partly be attributed to the weak interfacial bond between the brass matrix and lead particles. The weak interface might allow separation and void formation under plastic deformation. Wolfenden and Wright [25] investigated the temperature in the tool–chip interface and whether lead appeared in solid state or as a liquid in the cutting zone. They concluded that although the heating time of a chip in a metal cutting operation is extremely short, at cutting speeds above $v_c = 125$ m/min, the dispersed lead spheres in the material will melt at the end of the secondary shear zone. Such melting is expected to facilitate lubrication on the tool–chip interface and result in lower cutting forces. However, these tool temperatures were based on calculations using shear plane angle theory and were not explicitly measured.

(iii) Long tool life

In machining brass using cemented carbide tools, there is a large difference in hardness between the tool and the workpiece material. A low level of abrasive tool wear is expected, suggesting that diffusional wear or chemical wear controls tool life. Both of these degradation processes are highly dependent on cutting temperature and can be slowed by using protective coatings. Similar protection can be achieved if the tool–workpiece elements react in situ during the cutting process to form a protective reaction layer [26]. Formation of such a layer in machining lead-free brasses was observed earlier by Schultheiss et al. and Bushlya et al. [6, 14]. Both report that machining a lead-free silicon brass (CuZn21Si3P) leads to significantly shorter tool life compared to machining leaded brass (CuZn39Pb3). The tool temperatures reported in the literature [25, 27, 28] indicate the possibility that lead may melt in the secondary shear zone. If melting of lead occurs in the cutting zone, it can form a protective film between tool and chip, thus retarding diffusional or chemical wear processes. Samandi and Wise [27] measured tool temperatures based on microhardness measurements and microstructural changes in a cutting tool made of a tool steel (1% C, 1.5% Cr). Based on these measurements, the tool temperature at the end of the contact zone was found to be around 350 °C using a cutting speed of 120 m/min for leaded brass. However, these results for tool steel may not be transferable to today's industrial cemented carbide tools, which have different properties and tribological performance.

The literature thus agrees that lead benefits the machining process, yet the exact mechanisms associated with these benefits are open for discussion. It is not clear whether lead melts during the machining process. If so, does it melt in the primary or secondary shear zone? Is the difference in cutting force due to tribology or mechanical properties? Nor is it known whether the effect originates in the primary or secondary deformation zone. Is the long tool life for leaded brass related to the formation of a diffusion barrier from the lead film on the cutting tool, or to the low temperatures caused by low force and short contact length?

This paper investigates differences in the machinability characteristics of two brass alloys, one with 3 wt.% lead (CuZn38Pb3) and one lead-free (0.1 wt.%) variant, CuZn42. A variety of techniques were employed to investigate the effect of lead, including infrared temperature measurement, cutting force measurements, electron microscopy, secondary ion mass spectroscopy, quick-stop methods, and high-speed filming.

Table 1 Measured chemical composition (wt.%) of the workpiece materials used

Alloy	EN code	Cu	Zn	Pb	Sn	Fe	Al	Ni	Mn	Si	As
CuZn39Pb3	CW614N	Rest	38.8	3.3	0.15	0.19	0.027	0.08	0.013	0.02	0.03
CuZn42	CW510L	Rest	42.2	0.1	0.02	0.09	–	0.01	–	–	0.01

Fig. 1 SEM image and XEDS mapping of the microstructure for the brass alloys CuZn38Pb3 (left) and CuZn42 (right) used
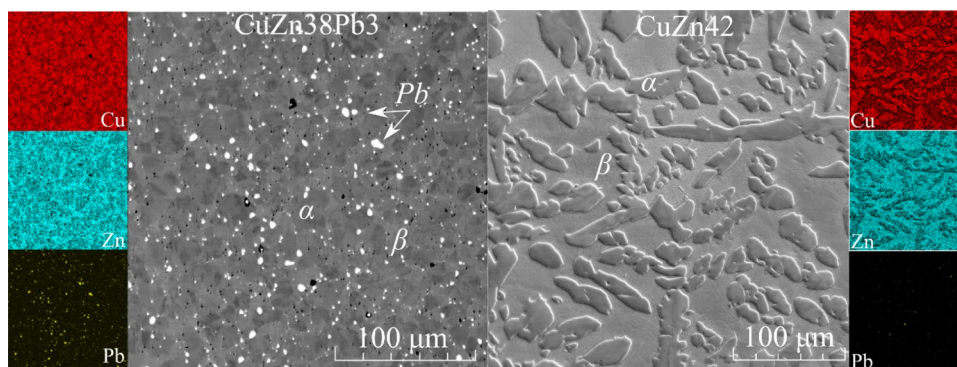
2 Experimental setup

The brass materials chosen for the study are very similar in their chemical composition and phase content, apart from the presence of lead, see Table 1 and Fig. 1. Both materials are commonly used by brass manufacturing industries in applications with low to medium demands on dezincification resistance. The lead-containing alloy CuZn38Pb3 consists of three cubic faces: (i) a copper-rich face-centered cubic phase, α (a = b = c = 0.370 nm) with the standard formula Cu0.67Zn0.33, (ii) a body-centered cubic phase, β (a = b = c = 0.296 nm) with the standard formula CuZn, and (iii) pure lead [29]. In Fig. 1a, the lead phase is clearly identifiable as white inclusions in the CuZn38Pb3 alloy. The same phases, except for the pure lead, can be found in the lead-free material CuZn42. The proportions of α and β in the materials are similar, around 50%, but the grain size in CuZn42 is larger than in CuZn38Pb3.

In tensile tests performed in accordance with ISO 6892–1, the materials perform alike (Fig. 2), reporting nearly identical average values of ultimate tensile strength and ductility, and similar yield strength ($R_{\text{p}02}$). However, the similarity in mechanical properties does not translate into a similarity in cutting resistance. A series of force measurements in turning

operations with varying feed f or undeformed chip thickness h_1 ($f = 0.05$ mm/rev to $f = 0.3$ mm/rev) was conducted while keeping other process parameters fixed: depth of cut $a_p = 2$ mm and cutting speed $v_c = 200$ m/min. The cutting tool was an uncoated cemented carbide insert with neutral geometry ($\gamma = 0$ deg.) and a nose radius of 0.8 mm. In production of brass components, it is common to use complex uncoated cemented carbide tools, i.e., form tools and step drills, which typically are used with a neutral geometry. The measured values of cutting resistance agree well with both the Woxén-Johansson [30, 31] and Kienzle [32] models (Eq. 1–2). It can be seen (Fig. 3) that the leaded CuZn38Pb3 alloy shows approximately 50% reduction in cutting resistance over the lead-free variant:

$$C_r = \frac{F}{h_1 \cdot b_1} = Cr_1 + \frac{Cr_2}{h_1} \tag{1}$$

$$k_c = k_{c1.1} \cdot h_1^{-m_c} \tag{2}$$

The average cutting forces were measured using a Kistler 9129 AA force dynamometer. The dynamic cutting forces were measured by a center-in-line force sensor designed and built at the Department of Mechanical Engineering Sciences
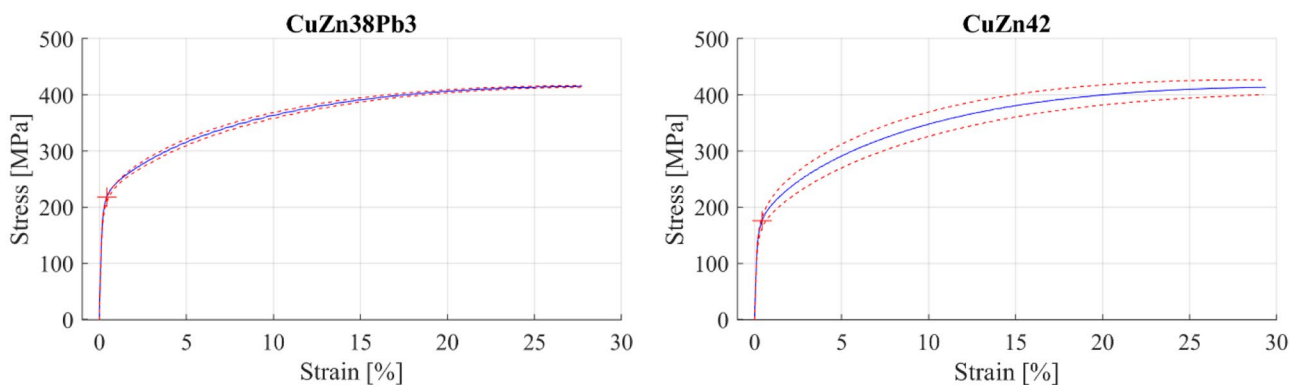

Fig. 2 Stress–strain curves for the tested materials. The blue line shows the average of three tensile tests, and the red dashed lines show one standard deviation from the average value. The cross marks $R_{\text{p}02}$
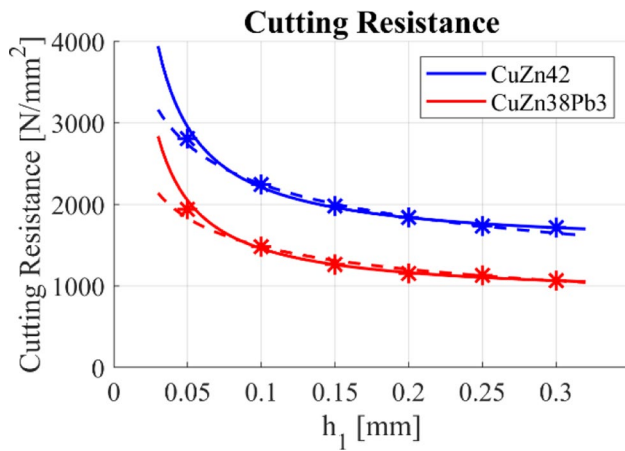
Cutting Resistance

Fig. 3 Cutting resistance for the materials used. The stars indicate measurement points, the solid lines show the Woxén-Johansson model, and the dashed lines show the Kienzle model

at Lund University [33, 34]. The force sensor has a high eigen-frequency and thus allows high sampling rates during the measurement. In this study, the sampling rate was 200 kHz.

The temperature in the cutting zone was measured using thermal imaging [35, 36]. The tool temperature measurements were performed during orthogonal turning of disk-shaped workpieces, as shown in Fig. 4 (left). The depth of cut (disk thickness) $a_p = 2$ mm and the cutting speed $v_c = 200$ m/min were kept constant, but the feed varied from $f = 0.05$ to 0.2 mm/rev. An infrared thermal camera (FLIR X6580sc with a T198970 lens) was set up to capture the side of the cemented carbide tool at 200 frames per second. The tool was positioned 0.15 mm outside the disk on the camera side (tool offset) to avoid uncut material and burrs covering the camera's view. The emissivity of the cemented carbide tool was set to 0.3 as determined by separate two color pyrometer and thermocouple tests.
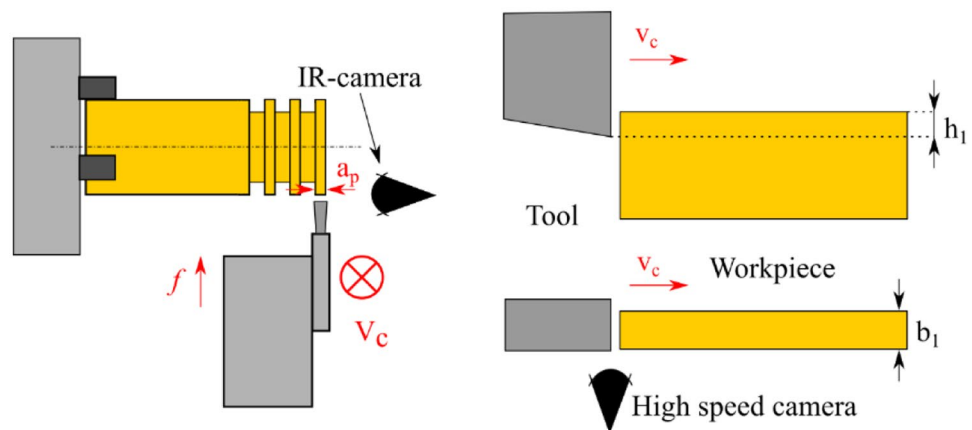
High-speed filming of the chip formation process also involved the orthogonal cutting setup. A camera was installed in a planing machine with a stationary tool and moving workpiece, see Fig. 4 (right), and set up to image at 30,000 frames per second. Experimental conditions involved a variation of both the cutting speeds and the theoretical chip thicknesses h1.

Both the IR and high-speed imaging document the phenomena occurring on the side surface of the tool or the workpiece material and do not examine what is happening inside the cutting zone. The latter was achieved using a quick-stop device whose schematic is shown in Fig. 5. During machining, a striker M is accelerated toward the tool by a gunpowder charge. Upon impact, the tool will pivot and break the shear pin, thereby disengaging from the workpiece. The chip root obtained is subsequently cross-sectioned and polished to reveal chip formation, microstructural changes, and the deformation zones within the chip εI, at the tool–chip interface εII, and at the tool–workpiece interface εIII.

The analysis of the function of lead also employed several microscopy and spectroscopy techniques. A Tescan Mira3 high-resolution Schottky FE-SEM was used for scanning electron microscopy (SEM) and X-ray energy dispersive spectroscopy (XEDS). Surface-sensitive compositional measurements were performed using Secondary Ion Mass Spectrometer with a Time-of-Flight detector (ToF–SIMS) (mod. IONTOF V) used to determine the chemistry of the surface of the cutting tool. A Bi3 beam at 25,000 eV beam was used for these measurements using the macro stage raster function to analyze a 1500 μm × 1500 μm area.

3 Results and discussion

The tool temperature measured with the IR imaging setup showed that for all tested cutting conditions, the temperature when machining CuZn38Pb3 is much lower than the temperature when cutting lead-free CuZn42 alloy, see Fig. 6. For

Fig. 4 Experimental setup for IR thermal imaging (left) and experimental setup for high-speed filming (right)

Fig. 5 Schematic of the quick-stop device (left) and polished chip root cross-section with the different deformation zones marked (right)
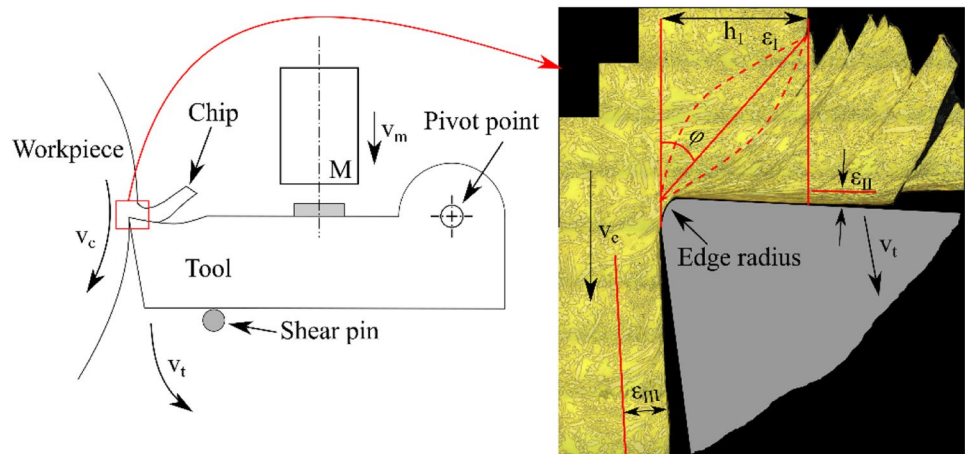
vc = 200 m/min, f = 0.2 mm/rev, and ap = 2 mm (Fig. 7), the highest measured tool temperature for CuZn38Pb3 is around 180 °C, which is significantly lower than the melting temperature of lead (Tmelt, Pb = 328 °C) [37]. It is also interesting that the highest temperature is observed in the vicinity of the cutting edge or directly on the edge radius. The lead-free brass CuZn42 has nearly double the tool temperature, around 360 °C, under identical cutting conditions. In addition, the hottest region is located behind the cutting edge, indicating a longer tool–chip contact length compared to machining CuZn38Pb3. The observed higher tool temperature can, in part, explain the shorter tool life reported for lead-free brass.

Figure 7 reports tool and tool–chip interfacial temperature. However, it is more difficult to measure the chip temperature because it relies on the emissivity of the brass alloy. For brass alloys, emissivity ranges $\varepsilon = 0.03$–0.5 [38] are reported. The lowest values occur for polished surfaces and strongly increase with increasing surface roughness, degree of oxidation, and the temperature itself [39]. During

machining, the side of the chip simultaneously experiences a varying degree of change in roughness and oxidation, thus making the thermal data from chips drastically unreliable.

As already indicated by the thermal imaging, the tool–chip contact length appears to be different. High-speed filming shows the same trend as thermal imaging, but at more accurate temporal and spatial resolution. Figure 8 shows that for the leaded brass CuZn38Pb3, the chip is separated from the workpiece as discrete segments, unlike the chips produced from CuZn42 where the chip is segmented but continuous. As for the contact length, for CuZn38Pb3 brass, it is comparable with the theoretical chip thickness and ranges lr = (0.6–1.0)•h1, while for CuZn42 brass, it is more than double, namely, lr = (1.7–2.2)•h1.

More remarkable is that the segmented chip formation for CuZn38Pb3 is independent of cutting speed, as seen in Fig. 9. Even at cutting speeds as low as 12 m/min, the chip formation follows the typical segmentation sequence of compression by the tool followed by deformation along the shear plane [40]. However, in this case, segment separation takes place. Such chip segmentation at low speed indicates that the short chipping of leaded brass is not controlled by temperature in the primary deformation zone and precludes the melting of lead on the interface between the chip segments. A more likely concept for the chip formation is presented by Doyle [20], who investigated the plastic instabilities that can arise in heterogeneous materials. Lead has nearly a 10 times lower Young's modulus and 20 times lower strength than the matrix brass alloy [41].

From the high-speed footage for CuZn38Pb3, it appears that the tool practically loses contact with the workpiece on the rake side when a chip segment separates from the workpiece. By measuring the dynamics of the cutting forces with a high sampling frequency (200 kHz) for a cutting dataset of vc = 150 m/min, f = 0.4 mm/rev, and ap = 2 mm, the differences between the machining of the two brass alloys become
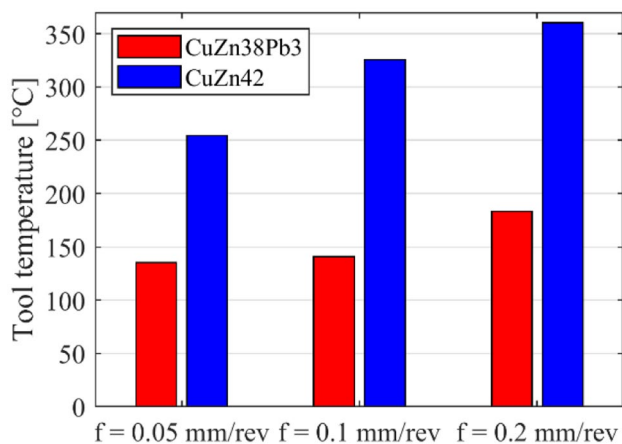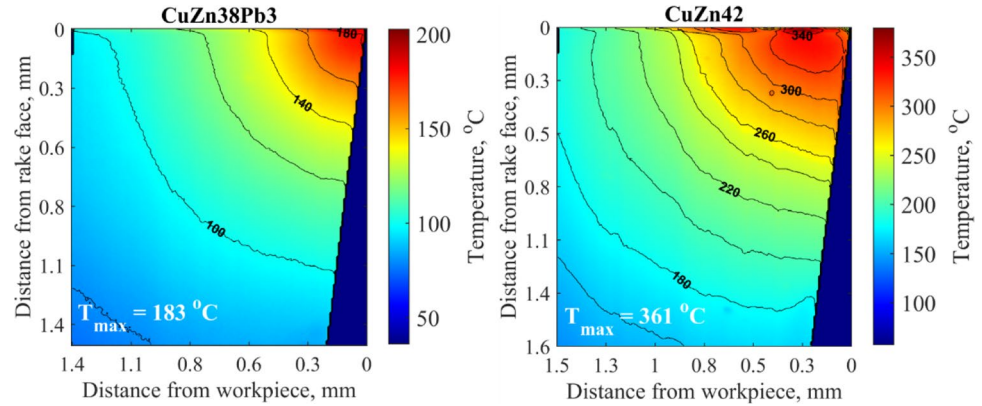

Fig. 6 Maximum tool temperature for the two alloys at different feeds measured with IR-camera

Fig. 7 Tool temperature for CuZn38Pb3 (left) and CuZn42 (right) obtained by IR thermal imaging during machining. (Note the difference in temperature scale.)

apparent, see Fig. 10. While the peak force for the lead-free material is slightly higher than for the CuZn38Pb3 alloy, the variation in the cutting forces is dramatically different between the alloys. For the leaded brass, the cutting force is almost sinusoidal and is $Fc = 554 \pm 514$ N, whereas for the lead-free brass, it is $Fc = 1154 \pm 263$ N, and only small peaks related to the chip formation process are observed. The force pattern for the lead-free CuZn42 alloy follows the traditional sequence of a segmented (saw-tooth) chip formation cycle [42]. Here, the material ahead of the cutting edge is compressed, resulting in increased forces, followed by shear initiation, shear localization, adiabatic heating, and segment formation, all resulting in a force reduction. Apparently, in the case of leaded CuZn38Pb3 alloy, the end result of cyclically increased and reduced forces is similar, but the causes might not be identical. The analysis of the force and high-speed footage reveals that the compression stage is the same, but upon shear initiation, a plastic instability promoted by the lead rapidly localizes the shear process to the degree that a segment detaches from the material bulk. Each individual segment is then ejected by the oncoming tool and stored elastic strain, thus producing discontinuous chips.

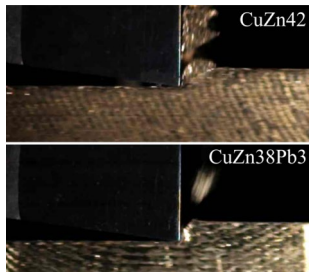While the peak value of the cutting force component Fc is similar for both alloys, the peak value of the feed force Ff is almost halved for the leaded CuZn38Pb3 alloy. It seems that a compression cycle, which is similar for both alloys, contributes to the similarity in the cutting force component Fc. Feed force Ff, on the other hand, is to a higher degree controlled by the tribology of the tool–chip contact on the rake. The tool temperature at high cutting speeds is evidently lower for the leaded brass (Fig. 7). Several explanations have been offered for this lower temperature, including the low friction on the rake. Some authors [25, 28] suggest that melting lead has a significant lubricating effect that enhances the machinability. Thermal softening and melting of lead, and thus its lubricating efficiency, are temperature dependent. Varying the cutting speed is a controllable process parameter that has a direct effect on the process temperature.

A series of machining experiments within the speed range of vc = 2 m/min to 100 m/min were conducted to evaluate the effect of lead on cutting forces and the friction coefficient. All tests were performed using a constant depth of
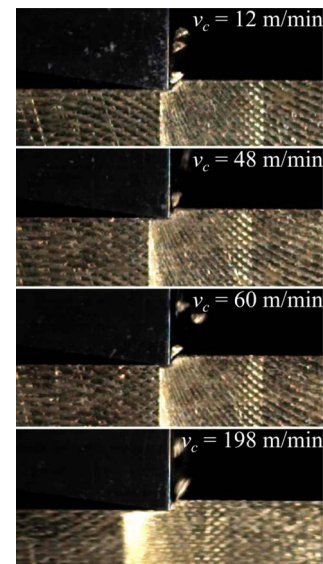
Fig. 8 Optical image frames from high-speed filming showing the chip formation and tool–chip contact length for CuZn42 and CuZn38Pb3 (vc = 198 m/min, h1 = 0.4 mm, b1 = 3.5 mm)

Fig. 9 Chip formation during machining CuZn38Pb3 alloy at different cutting speeds (h1 = 0.2 mm, b1 = 3.5 mm)

Fig. 10 Dynamic cutting forces measured at 200 kHz for leaded (left) and lead-free brass (right) plotted over 5 ms (vc = 150 m/min, f = 0.4 mm/rev, ap = 2 mm)
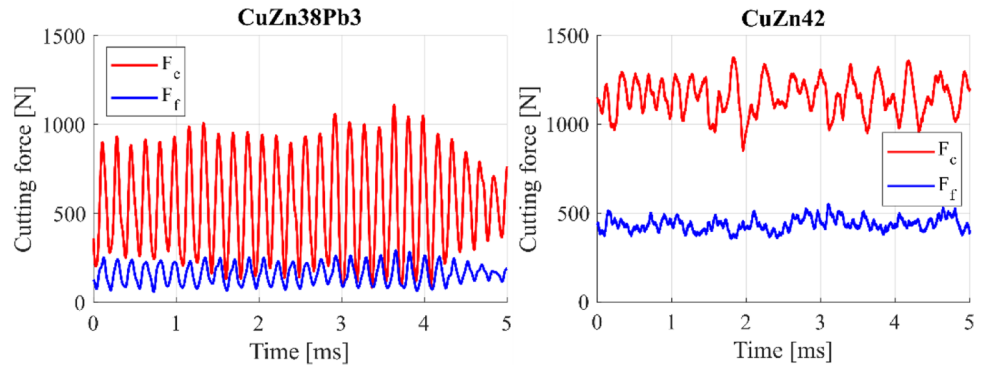
cut, ap = 2 mm. The results that can be seen in Fig. 11b, d show that the cutting forces for both brass alloys are largely independent of the cutting speed. However, the force level is higher for CuZn42 than for CuZn38ZnPb3 under all conditions. It is worth noting that machining CuZn38Pb3 alloy resulted in a consistent artifact in force behavior. This artifact consists of a strong variation in forces at particular speed ranges, which depended on the feed used. For feed f = 0.1 mm/rev, this variation was observed at vc = 30 m/min,

it increased to vc = 60 m/min at f = 0.2 mm/rev, and further shifted to vc = 80 m/min at f = 0.3 mm/rev. The most likely source of the variation is vibration or chatter. To eliminate this effect, the experiments were repeated with different set-ups, and even on another lathe with a force measurement system, designed for the lathe and built by Kistler, yet all yielded similar results. An alternative explanation is that the formation of a built-up edge (BUE) might influence the forces. However, analysis of the machined surfaces and the
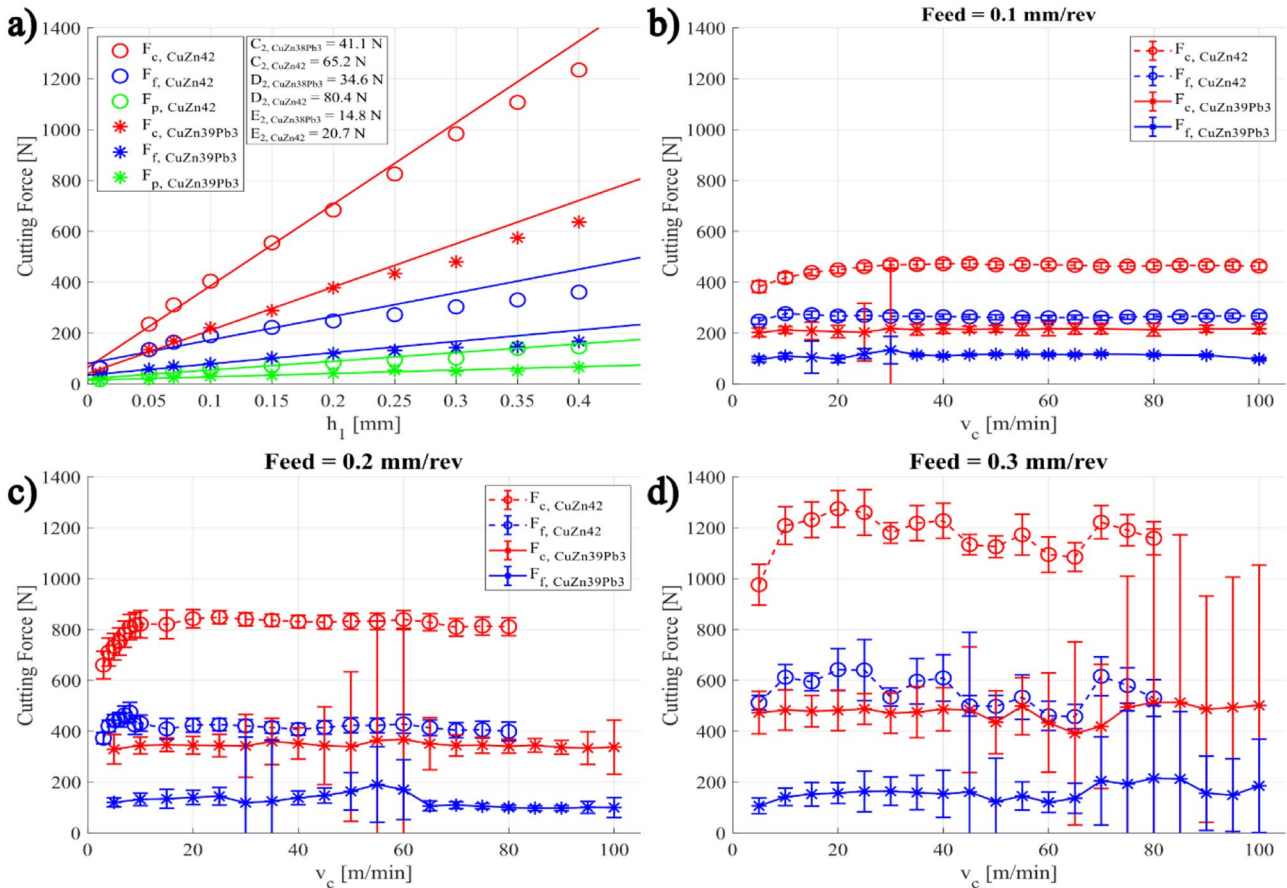
Fig. 11 The cutting forces for both brass alloys are largely independent of the cutting speed
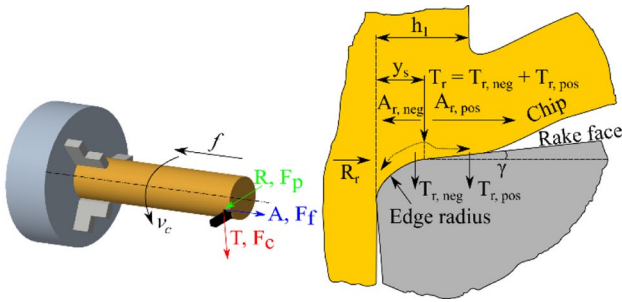
Fig. 12 Definition of main directions and force directions in a general turning process and a section of an engaged tool with the forces that act on the rake face of a cutting tool. Modified after Ståhl [17] and Schultheiss [44]

cutting tools revealed an absence of BUE. The consistency of the observed phenomenon calls for further investigation.

Estimation of the coefficient of friction on the tool-chip interface requires separating the force components acting on the rake and the flank side of the tool. It is sometimes often in the cases of rough machining, considered that forces on the flank can be neglected and the coefficient of friction is simply a ration of feed to cutting forces: $\mu = F_f/F_c$ [43]. In practice, the workpiece material flowing against the tool is separated into two separate flows by the cutting edge. The point where the material flow is separated is located in the vicinity of the edge radius and is called the stagnation point (see Fig. 12). The material below stagnation point moves toward the tool's clearance side, is ploughed under the edge, and is not removed from the workpiece. Ploughing forces involved in this action do not contribute to the normal and frictional forces on the tool rake side. Similarly, the rubbing action of the tool clearance against the machined workpiece material adds to the clearance forces.

These forces are easily found by extrapolating the feed or chip thickness values for h1 = 0 [45]. Therefore, the total force can be described by the following, where C2, D2, and E2 are the forces acting on the clearance side.

$$F_c = C_2 + C_1 \cdot h_1 = T_r + T_{cl}$$
$$F_f = D_2 + D_1 \cdot h_1 = A_{cl} + A_r \qquad (3)$$
$$F_p = E_2 + E_1 \cdot h_1 = R_r + R_{cl}$$

Figure 11 a shows the linearization of the cutting forces necessary to determine C2, D2, E2, and their values. From Fig. 12 and Eq. 4, it is possible to derive and calculate an estimate of the coefficient of friction based on the measured cutting forces, by slightly altering the model presented by Schultheiss [44] to accommodate the contribution to friction from Fp, Eq. 4. The apparent coefficient of friction will be an indicator of how much lead contributes to reducing friction and thereby the cutting forces:

$$\mu_r = \frac{\sqrt{A_r^2 + R_r^2}}{T_r} = \frac{\sqrt{\left(F_f - D_2\right)^2 + \left(F_p - E_2\right)^2}}{F_c - C_2} \qquad (4)$$

The calculation results for the apparent coefficient of friction are shown in Fig. 13. For the lead-free alloy CuZn42 (on the right), the apparent coefficient of friction μr is between 0.39 and 0.57 and is relatively constant over the considered range of cutting speed and the feed. The same cannot be said about machining CuZn38Pb3. While the change in μr over the speed range can be related to the force artifact mentioned above, there is also a strong dependency on the feed. At feed f = 0.1 mm/rev, the apparent coefficient of friction is μr = 0.45, and it reduces to μr = 0.24 at feed f = 0.3 mm/rev. On the one hand, an expected increase in process temperature with an increased feed should facilitate softening of Pb, increased lubrication efficiency, and thus a lower friction coefficient. On the other hand, an increase in the cutting speed should also increase the process temperature and thus produce similar effects, yet the data shows that increasing speed does not reduce μr.

Fig. 13 Apparent coefficient of friction for the two brass alloys
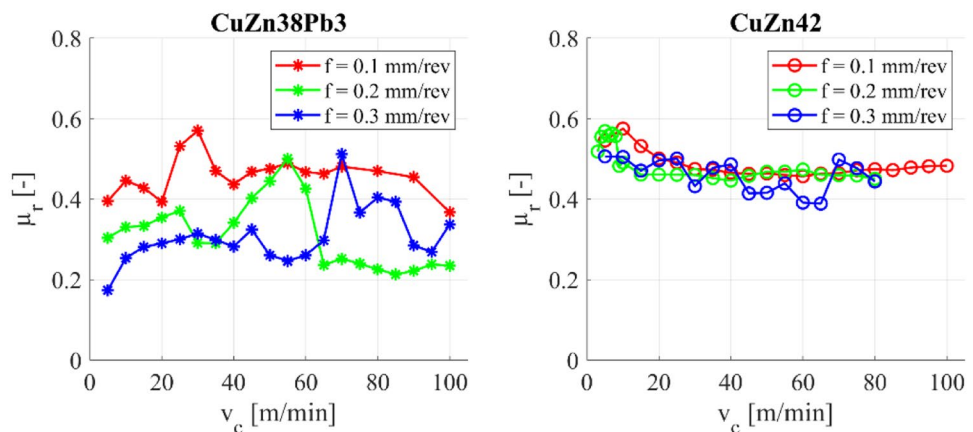
The surface chemistry within the contact region was analyzed in an attempt to detect the impact of lead on the friction and tribology, because the mechanistic explanation appears to be contradictory. An uncoated cemented carbide tool was used to machine CuZn38Pb3 for 3 min at vc = 200 m/min, f = 0.2 mm, and ap = 1.5 mm. SEM and XEDS data (see Fig. 14) do show the presence of lead on the rake face, but not in the contact zone between the tool and the chip. The Lα energy level for lead is 10.55 keV, and thus, XEDS maps were made using an acceleration voltage of 20 kV for accuracy of quantification. Using such high voltage for XEDS analysis means that the excitation volume also includes the bulk material and probably underestimates the data for thin surface layers such as the lead monolayer reported by Stoddart et al. [23].

To further study the chemical composition of the tool–chip interface, time-of-flight secondary ion mass spectrometry (ToF–SIMS) was used (see Fig. 15) because the method is sensitive to the top-most layers of a tool sample. The same tool was examined using both XEDS and ToF–SIMS. As with the XEDS, high levels of lead were found outside the theoretical contact area, but ToF–SIMS reveals that the copper from the workpiece material covers nearly the entire contact zone. Lead is detectable in the part of the contact area furthest from the edge line. Using the analogy of the common sticking and sliding regions found on cutting tools [46, 47], lead is not present in the sticking region, but is slightly present in the sliding region. As shown in the high-speed footage, Figs. 8 and 9, the tool–chip contact length for CuZn38Pb3 is very short and approximately equal to the theoretical chip cross-section profile. The footage also reveals that there is no sliding region in its conventional form. Therefore, it can be assumed that the lead within the contact zone stems from rubbing of chips after separation from the workpiece, and the lead outside the contact zone is from the particles ejected from the chips. Since the area affected by lead is small (approximately 10%) compared to the entire tool–chip contact zone, the effect of
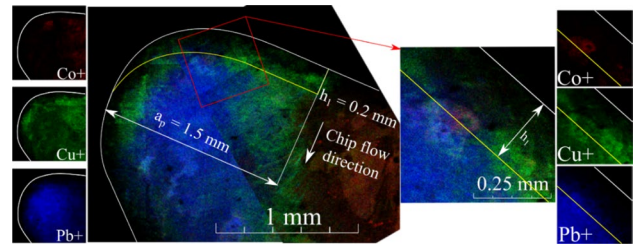

Fig. 15 Chemical composition on the rake surface captured by ToF–SIMS after three minutes of machining CuZn38Pb3. The theoretical contact area is marked with a yellow line

Pb on the frictional forces and its likely lubrication effect can be considered minor.

As there is no evidence supporting either melting of lead or lead's lubricating effects on the tool–chip interface, attention turned to the workpiece to find the mechanisms behind the high machinability of the alloy. Quick-stop samples were prepared as shown in Fig. 5 in order to follow the path of the lead through the cutting zone. The quick-stop samples for both alloys were generated in longitudinal turning at vc = 70 m/min, f = 0.4 mm/rev, and ap = 2 mm and are shown in Fig. 16 before cross-sectioning. As can be seen, the CuZn38Pb3 quick-stop sample has chip segments formed but partly attached, while the other segment is in the compression stage. For the lead-free case, the attached chip is continuous, with clear saw-tooth morphology.

After extraction and polishing of the quick-stop samples, the differences between the cutting zones of the two alloys can be seen in Figs. 17 and 18. The chip root of the CuZn42 alloy is characterized by segmentation, with larger segments separated by shear bands alternating with smaller peaks. The shear bands are very thin (5–15 μm), some even underdeveloped. The secondary εII and tertiary εIII deformation zones, on the other hand, are very substantial: εII ≈ 100 μm and εIII ≈ 150 μm. This is indicative of higher contact loads on the tool–chip and tool–workpiece interfaces and is consistent
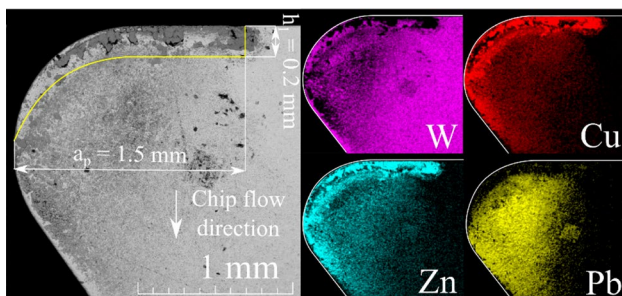

Fig. 14 Backscattered SEM image and XEDS maps of the rake face after 2 min of machining CuZn38Pb3. The theoretical chip contact area is marked by a yellow line
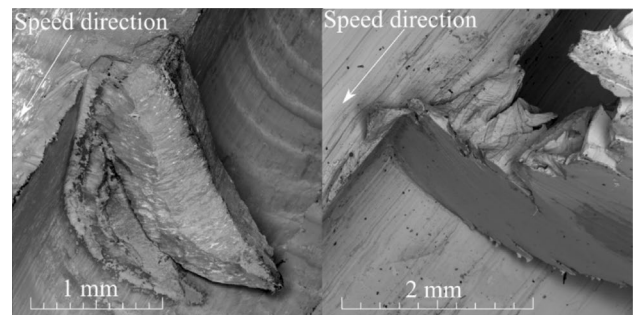

Fig. 16 Quick-stop samples of CuZn38Pb3 (left) and CuZn42 (right) before grinding and polishing
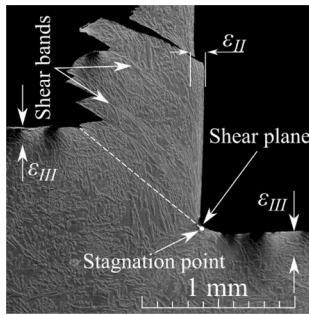
Fig. 17 Quick-stop samples of CuZn42 with interesting regions marked

Fig. 19 Close up of the primary shear zone of CuZn38Pb3 combined with XEDS maps

with the higher forces and friction observed for this alloy (see Figs. 11 and 13).

The chip root of CuZn38Pb3 alloy exhibits a different morphology with a distinct and wide shear band and the expected segment separation. Unexpectedly, secondary and tertiary deformation zones are large: εII ≈ 100 μm and εIII ≈ 50 μm as can be seen by elongation of brass and lead grains. The primary deformation zone is also very wide (εI ≈ 100–150 μm), where the lead grains are strongly textured and parallel to the shear plane, as compared to the unaffected microstructure shown in Fig. 1. A more detailed image of the primary shear zone can be seen in Fig. 19, in combination with XEDS maps for relevant elements. The elongated and flake-like lead grains are clearly visible as bright spots in the backscatter image. Additionally, in the XEDS map, an agglomeration of lead on both sides of the shear plane is clearly distinguished. As previously discussed, high excitation voltage during XEDS analysis will read the signal from sub-surface layers not visible in the backscatter mode. The agglomeration of lead near the shear plane may stem from a high concentration of lead on the shear plane itself.

While the sides of the shear plane are not visible in cross-section as seen in Fig. 19, this information can be found on the chips. Figure 20 shows that lead is indeed elongated and smeared all over the chip side of the shear plane.

The same traces of smeared lead found on the shear plane can be found on the machined surface, see Fig. 21. The layer of lead found on the machined surface is, however, very thin
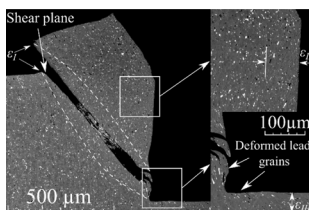
and is mostly visible when using a relatively low acceleration voltage in the SEM. At high acceleration voltage of 20 kV, only the elongated lead grains are distinguished, while at low voltage of 5 kV, lead covers nearly the entire surface. Smearing of lead on machined surfaces is documented in the literature [27, 48]. From a product point of view, smearing and redistribution of lead across the entire machined surface are more problematic than the presence of localized inclusions. It is known that the lead may leach into water and create adverse health and environmental effects [2–4]. The extensive surface coverage by the lead (Fig. 21) may create a spike in lead leaching and exposure during the initial stage of product use and cause more harm than estimated for the bulk case.

Our findings suggest that neither melting of lead nor lubrication and thus low friction across the tool–chip interface occur when machining leaded brass. Instead, the observations, as summarized graphically in Fig. 22, show that the low cutting forces are largely due to deformation of the segregated lead inclusions in the primary deformation zone. The highly deformed lead grains stretch along the shear plane, change shape from globular to flake-like inclusions, and act as crack initiation points in the brass matrix, so enforcing the process of discontinuous chip formation. The presented findings support Doyles [20] conclusion
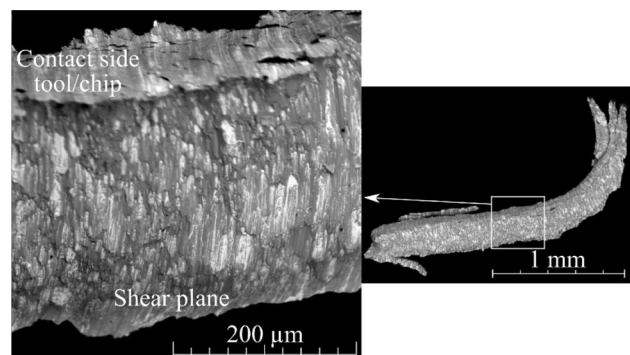

Fig. 18 Quick-stop samples of CuZn38Pb3 with interesting regions marked

Fig. 20 Backscatter image of the shear plane on a CuZn38Pb3 chip. Bright areas are lead
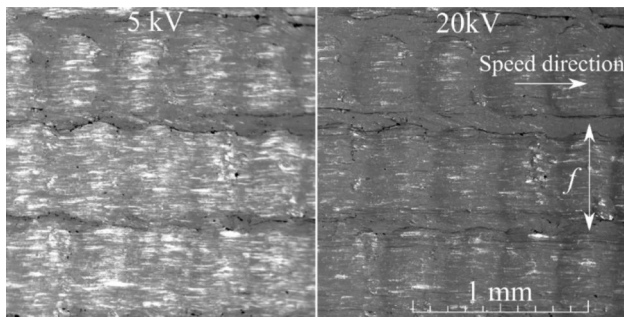
Fig. 21 Surface of machined CuZn38Pb3 captured in backscatter mode at the same location with different acceleration voltages, 5 kV (left) and 20 kV (right). Bright areas show lead

about mechanical instabilities causing discontinuous chip formation. This type of chip formation restricts the contact length between tool and chip (approximately 0.6–1.0•h1), resulting in low frictional forces and low tool temperature. Thermal measurements confirm that machining CuZn38Pb3 results in an approximately 180 °C lower tool temperature than machining CuZn42 (Fig. 7). Such low temperatures explain the extremely long tool life of cutting tools when machining brass with high lead content.

It is common to find the term "internal lubrication" being used to describe the beneficial effects of lead on the machining process [20, 22, 25, 28]. This term is often confusing as induced lubrication implies reduced friction. Our findings reveal that the lower apparent coefficient of friction for leaded brass is more dependent on chip formation, low tool–chip contact length, and subsequently lower feed force Ff, than on the lubricating effect of lead. In particular, atomic mono-layer resolution ToF–SIMS shows that lead is sparse on the tool surface in the contact zone, see Fig. 15. For these reasons, the term "internal lubrication" may be misleading.
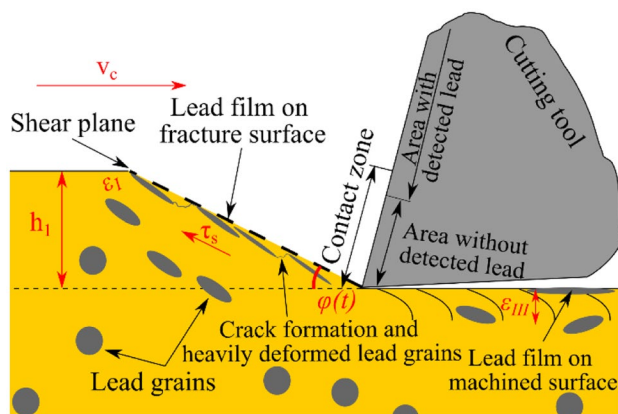

Fig. 22 Graphical summary of observed mechanism related to enhanced machinability of leaded brass alloys

4 Conclusions

High lead content makes brass alloys more machinable, but these alloys are not allowed in certain applications due to regulations related to lead toxicity. This article investigates the function of lead in providing high machinability.

Infrared temperature measurements when machining leaded (CuZn38Pb3) and lead-free (CuZn42) brasses found that the process temperature is below the melting point of lead, this finding thus excludes this commonly assumed mechanism. High-speed filming corroborated this observation, showing that segmented chip formation takes place even at speeds as low as $v_c = 12$ m/min. The same effect was observed when extending the speed range down to $v_c = 2$ m/min, low enough to exclude thermal effects. Instead, radical differences in tool–chip contact were observed for the two alloys. During machining, leaded brass has less than half the tool–chip contact length and a lower friction coefficient than unleaded brass. Analysis of the tool contact area with electron microscopy and spectrometry (ToF–SIMS) revealed lead had little effect on the contact conditions at the tool rake face. Using a quick-stop device to interrupt the machining process allowed the chip roots from both alloys to be studied. This revealed the contribution of lead to the chip formation mechanisms within the primary deformation zone. Lead changes its shape from globular to flake-like as the material passes through the primary deformation zone. These flakes are further stretched as they reach the shear plane and then act as crack initiation points, thus ensuring the formation of discontinuous chips. This effect prevents the development of stable tool–chip contact, thus lowering cutting forces, friction, and process temperature. Development of lead-free alloys with high machinability should therefore be focused on controlling chip formation rather than the tribological aspects of cutting.

Author contribution Jakob Johansson: conceptualization, validation, investigation, methodology, formal analysis, funding acquisition, writing—original draft. Per Alm: formal analysis, investigation, resources. Rachid M'Saoubi: formal analysis, investigation, resources. Per Malmberg: investigation, resources. Jan-Eric Ståhl: funding acquisition, validation, writing—original draft. Volodymyr Bushlya: conceptualization, investigation, methodology, supervision, validation, writing—original draft.

action for Metallic Materials, organized by Vinnova and Jernkontoret (Sweden) under the Optibrass project (ID 2019–02933) and the Sustainable Production Initiative (SPI), a collaboration between Lund University and Chalmers Institute of Technology.

Availability of data and material The raw/processed data required to reproduce these findings cannot be shared at this time as the data also forms part of an ongoing study.

Declarations

Ethics approval Not applicable.

Consent to participate Written informed consent for publication was obtained from all participants.

Consent for publication Written informed consent for publication was obtained from all participants.

Conflict of interest The authors declare no competing interests.

References

1. Vilarinho C, Davim JP, Soares D, Castro F, Barbosa J (2005) Influence of the chemical composition on the machinability of brasses. J Mater Process Technol 170(1–2):441–447. https://doi.org/10.1016/j.jmatprotec.2005.05.035

2. Mudipalli A (2007) Lead hepatotoxicity & potential health effects. Indian J Med Res 126(6):518–27. https://www.ncbi.nlm.nih.gov/pubmed/18219078

3. Mushak P (1992) Perspective. Environ Res 59(2):281–309. https://doi.org/10.1016/s0013-9351(05)80036-2

4. Rosner D (2016) A lead poisoning crisis enters its second century. Health Aff (Millwood) 35(5):756–759. https://doi.org/10.1377/hlthaff.2016.0362

5. Johansson J, Persson H, Ståhl JE, Zhou JM, Bushlya V, Schultheiss F (2019) Machinability evaluation of low-lead brass alloys. Procedia Manufacturing 38:1723–1730. https://doi.org/10.1016/j.promfg.2020.01.102

6. Schultheiss F, Johansson D, Bushlya V, Zhou J, Nilsson K, Ståhl J-E (2017) Comparative study on the machinability of lead-free brass. J Clean Prod 149:366–377. https://doi.org/10.1016/j.jclepro.2017.02.098

7. Nobel C, Klocke F, Lung D, Wolf S (2014) Machinability enhancement of lead-free brass alloys. Procedia CIRP 14:95–100. https://doi.org/10.1016/j.procir.2014.03.018

8. Amaral L, Quinta R, Silva TE, Soares RM, Castellanos SD, de Jesus AMP (2018) Effect of lead on the machinability of brass alloys using polycrystalline diamond cutting tools. J Strain Anal Eng Des 53(8):602–615. https://doi.org/10.1177/0309324718796384

9. Martinez-Hernandez M, Juarez-Hernandez A, Gonzalez-Rivera C, Hernandez-Rodriguez MAL (2013) Bismuth segregation and crack formation on a free lead yellow brass tap. Eng Fail Anal 28:63–68. https://doi.org/10.1016/j.engfailanal.2012.10.002

10. Li S, Imai H, Umeda J, Fu Y, Kondoh K (2016) Investigation of high-strength lead-free machinable Cu40Zn duplex graphite brasses by powder metallurgy. Mater Sci Technol 32(17):1751–1756. https://doi.org/10.1080/02670836.2016.1246098

11. Atsumi H, Imai H, Li S, Kondoh K, Kousaka Y, Kojima A (2011) High-strength, lead-free machinable α–β duplex phase brass Cu–40Zn–Cr–Fe–Sn–Bi alloys. J Materials Science Engineering: A 529:275–281. https://doi.org/10.1016/j.msea.2011.09.029

12. Laakso SVA, Hokka M, Niemi E, Kuokkala V-T (2013) Investigation of the effect of different cutting parameters on chip formation of low-lead brass with experiments and simulations. Proceedings of the Institution of Mechanical Engineers, Part B: Journal of Engineering Manufacture 227(11):1620–1634. https://doi.org/10.1177/0954405413492732

13. Toulfatzis A, Pantazopoulos G, David C, Sagris D, Paipetis A (2018) Machinability of eco-friendly lead-free brass alloys: cutting-force and surface-roughness optimization. Metals 8(4):250. https://doi.org/10.3390/met8040250

14. Bushlya V, Johansson D, Lenrick F, Ståhl J-E, Schultheiss F (2017) Wear mechanisms of uncoated and coated cemented carbide tools in machining lead-free silicon brass. Wear 376–377:143–151. https://doi.org/10.1016/j.wear.2017.01.039

15. Klocke F, Nobel C, Veselovac D (2015) Influence of tool coating, tool material, and cutting speed on the machinability of low-leaded brass alloys in turning. Mater Manuf Processes 31(14):1895–1903. https://doi.org/10.1080/10426914.2015.1127944

16. Williams JE, Smart EF, Milner DR (1970) Metallurgy of machining 2. Cutting of single- phase, 2-phase and some free machining alloys (article). Metallurgia 81(484):51–59. https://www.webofscience.com/wos/woscc/full-record/WOS:A1970F675100004?SID=EUW1ED0F2EXy6lbj8pPA62Qn1fvK2

17. Ståhl JE (2012) Metal cutting theories and models. Division of Production and Materials Engineering

18. Jaspers SPFC, Dautzenberg JH (2002) Material behaviour in metal cutting: strains, strain rates and temperatures in chip formation. J Mater Process Technol 121(1):123–135. https://doi.org/10.1016/s0924-0136(01)01227-4

19. Hofmann U, El-Magd E (2005) Behaviour of Cu-Zn alloys in high speed shear tests and in chip formation processes. Mater Sci Eng, A 395(1–2):129–140. https://doi.org/10.1016/j.msea.2004.12.030

20. Doyle ED (1974) Mechanisms of plastic instability in the machining of metals

21. Laakso SVA, Johansson J, Johansson D, Schultheiss F, Ståhl J-E (2019) Multi-objective testing of different brass alloy components for DFM. Procedia CIRP 81:127–132. https://doi.org/10.1016/j.procir.2019.03.023

22. Kuyucak S, Sahoo M (1996) A review of the machinability of copper-base alloys. Can Metall Q 35(1):1–15. https://doi.org/10.1179/cmq.1996.35.1.1

23. Stoddart CTH, Lea C, Dench WA, Green P, Pettit HR (1979) Relationship between lead content of Cu–40Zn, machinability, and svvarf surface composition determined by Auger electron spectroscopy. Metals Technology 6(1):176–184. https://doi.org/10.1179/030716979803276435

24. Gane N (1980) The effect of lead on the friction and machining of brass. Philos Mag A 43(3):545–566. https://doi.org/10.1080/01418618108240394

25. Wolfenden A, Wright PK (1979) Role of lead in free-machining brass. Metals Technology 6(1):297–302. https://doi.org/10.1179/030716979803276697

26. Bjerke A, Hrechuk A, Lenrick F, Markström A, Larsson H, Norgren S et al (2021) Thermodynamic modeling framework for prediction of tool wear and tool protection phenomena in machining. Wear 484–485:203991. https://doi.org/10.1016/j.wear.2021.203991

27. Samandi M, Wise M (1989) Machinability of copper based alloys. J INCRA Rep 110

28. Trent EM (1988) Metal cutting and the tribology of seizure: III temperatures in metal cutting. Wear 128(1):65–81. https://doi.org/10.1016/0043-1648(88)90253-0

29. 'Cu-Zn binary phase diagram 0–40 at.% Zn: datasheet from "PAULING FILE Multinaries Edition – 2012" in SpringerMaterials (https://materials.springer.com/isp/phase-diagram/docs/c_0906018) (2021) Springer-Verlag Berlin Heidelberg & Material Phases Data System (MPDS), Switzerland & National Institute for Materials Science (NIMS), Japan. Available at: https://materials.springer.com/isp/phase-diagram/docs/c_0906018 . (Accessed: 02 Dec 2021)

30. Woxén R (1932) A theory and an equation for the life of lathe tools. Ingeniörsvetenskapsakademins handlingar 119

31. Johansson I (1967) Metod för beräkning av skärkraft, moment och effekter vid fräsning. Chalmers tekniska högskola

32. Kienzle O (1952) Die bestimmung von kräften und Leistungen an spanenden Werkzeugen und Werktygsmaschinen (in German). J VDI-Z 94(11):299–305

33. Östholm S (1990) Simulering och identifiering av skäreggars mekaniska belastningsbild (in Swedish). Lund University, Doctoral

34. Ståhl JE, Östholm S 84–02 (1984) Studie av skäreggens belastningsbild vid diskontinuerlig spånbildning (in Swedish). Institutionen för mekanisk teknologi och verktygsmaskiners rapportserie. 1984–10–10. Lund, Sweden: Institutionen för mekanisk teknologi, Tekniska högskolan i Lund

35. Augspurger T, Bergs T, Döbbeler B, Lima A (2019) Methodology for the measurement of the heat partitioning by thermal imaging in the orthogonal cutting process. J Heat Transf 141(7). https://doi.org/10.1115/1.4043170

36. Davies MA, Ueda T, M'Saoubi R, Mullany B, Cooke AL (2007) On the measurement of temperature in material removal processes. CIRP Ann 56(2):581–604. https://doi.org/10.1016/j.cirp.2007.10.009

37. Predel B. 'Ac-Ag ... Au-Zr · Introduction: datasheet from Landolt-Börnstein - Group IV Physical Chemistry · Volume 12A: "Ac-Ag ... Au-Zr" in Springer Materials. Springer-Verlag Berlin Heidelberg. Available at: https://materials.springer.com/lb/docs/sm_lbs_978-3-540-33962-5_2

38. Rudnev V, Loveless D, Cook R, Black M (2003) Handbook of induction heating. Marcel Dekker Inc, New York, USA

39. Lanc Z, Zeljković M, Živković A, Štrbac B, Hadžistević M (2018) Determination of emissivity of brass alloy using infrared thermographic technique. Original scientific paper Izvirni znanstveni članki 65(3):115–122

40. Sagapuram D, Udupa A, Viswanathan K, Mann JB, M'Saoubi R, Sugihara T et al (2020) On the cutting of metals: a mechanics viewpoint. J Manuf Sci Eng 142(11). https://doi.org/10.1115/1.4047869

41. Thornton I, Rautiu R, Brush SM (2001) Lead the facts. London, UK: IC Consultants Ltd

42. Vyas A, Shaw MC (1999) Mechanics of saw-tooth chip formation in metal cutting (article). J Manuf Sci Eng 121(2):163–172. https://doi.org/10.1115/1.2831200

43. Shaw MC, Cookson JO (2005) Metal cutting principles. Oxford University Press, New York, Oxford, New York, USA

44. Schultheiss F, Fallqvist M, M'Saoubi R, Olsson M, Ståhl JE (2013) Influence of the tool surface micro topography on the tribological characteristics in metal cutting—part II Theoretical calculations of contact conditions. Wear 298–299:23–31. https://doi.org/10.1016/j.wear.2012.11.067

45. Ståhl J-E (1986) Skäreggars spontanhaverier. Lund University, Doctoral

46. Trent EM, Wright PK (2000) Metal cutting. Butterworth-Heinemann

47. Doyle ED, Horne JG, Tabor D (1979) Frictional interactions between chip and rake face in continuous chip formation (article). Proceedings of the Royal Society of London. A. Mathematical and Physical Sciences 366(1725):173–183. https://doi.org/10.1098/rspa.1979.0046

48. Chandrasekaran H, Granfors M, M'Saoubi R (2006) Tribological aspects of tool–chip and tool–work contact in machining and the application of laser spectrometry. Wear 260(3):319–325. https://doi.org/10.1016/j.wear.2005.04.023